

Design and Control of a Low-cost Non-backdrivable End-effector Upper Limb Rehabilitation Device

Fulan Li^{1,2}, Yunfei Guo¹, Wenda Xu¹, Weide Zhang¹, Fangyun Zhao¹, Baiyu Wang¹, Huaguang Du¹, and Chengkun Zhang¹

Abstract—This paper presents the development of an upper limb end-effector based rehabilitation device for stroke patients, offering assistance or resistance along any 2-dimensional trajectory during physical therapy. It employs a non-backdrivable ball-screw-driven mechanism for enhanced control accuracy. The control system features three novel algorithms: First, the Implicit Euler velocity control algorithm (IEVC) highlighted for its state-of-the-art accuracy, stability, efficiency and generalizability in motion restriction control. Second, an Admittance Virtual Dynamics simulation algorithm that achieves a smooth and natural human interaction with the non-backdrivable end-effector. Third, a generalized impedance force calculation algorithm allowing efficient impedance control on any trajectory or area boundary. Experimental validation demonstrated the system’s effectiveness in accurate end-effector position control across various trajectories and configurations. The proposed upper limb end-effector-based rehabilitation device, with its high performance and adaptability, holds significant promise for extensive clinical application, potentially improving rehabilitation outcomes for stroke patients.

Index Terms—Upper Limb Rehabilitation, End-effector Rehabilitation Robot

I. INTRODUCTION

Every forty seconds, an individual in the United States experiences a stroke, and every four minutes, a stroke leads to death. Approximately 7.6 million Americans aged 20 years and older have experienced stroke. As age progresses, the prevalence of stroke increases in both males and females. By 2030, the prevalence rate is projected to increase to 3.9% [1], making stroke a major health concern in the US. Research shows that between 30% to 66% of hemiplegic stroke patients experience limited arm motor function six months after a stroke, with only 5% to 20% demonstrating complete functional recovery [2]. These low patient recovery rates are linked to diminished quality of life and increased risks to overall well-being.

Robotic-assisted therapy (RAT) has been found to be a valuable adjunct to conventional physical therapy for post-stroke upper extremity rehabilitation, particularly for subacute stroke patients [8]. Compared to conventional physical therapy, RAT allows patients to undergo consistent and repetitive rehabilitation exercises, showing comparable and better outcomes [9]. Among those frequently researched RAT devices (e.g. rehabilitation exoskeletons and end-effector devices), the end-effector rehabilitation devices are particularly popular due to their portability and affordability. Meanwhile, the end-effector



Fig. 1. End-effector rehabilitation devices. (A) InMotion [3] arm rehabilitation device, commercialized based on the multi-link MIT MANUS [4] design. (B) H-MAN [5] arm rehabilitation device, utilizing an H-shaped differential pulley and belt mechanism. (C) Physiobot arm rehabilitation device using a backdrivable linear actuated mechanism [6]. (D) ArmMotus M2 Gen [7] rehabilitation device utilizing a backdrivable linear actuated mechanism.

devices can still deliver patient outcomes that are comparable to more complex systems such as exoskeleton robots [9]. The present article introduces the design and control of a low-cost end-effector rehabilitation device. The proposed device and control method shows the potential to offer tailored and long-term adaptive training for stroke patients, and extend the device’s product life span.

A. End-effector Upper Limb Rehabilitation Devices

End-effector upper limb rehabilitation devices refer to planar robots enabling movement along a 2D plane. Numerous prior studies have investigated rehabilitation techniques using these 2D planar robots through rigorous experimental methodologies [4]–[6], [10]–[13]. There are three primary types of end-effector rehabilitation robots: multi-link robots [4], [10]–[12], pulley-driven robots [5], [13], and linear actuated robots [6] (Fig. 1). The MIT MANUS is a well-known example of a multi-link rotary robot with a two-decade history [4]. Stability of the vertical force, resulting from the user placing their arm on the device, has been a notable concern for multi-link rotary robots. Despite their portable and backdrivable direct drive mechanisms providing high accuracy, maintaining this stability remains challenging [5]. Stability issues can be a major issue affecting user experience, motivation, engagement, and product adoption rate [14], [15]. Pulley-drive robots attempted

¹Engineer at Futronics (NA) Corporation, Pasadena, CA, USA.

²Fulan Li is the corresponding author (email: lfulan@vt.edu).

to employ a differential drive with pulleys and belts, to address the stability issues and improve dynamics calculation [5], [13], [16], [17]. However, the pulley-drive robots require high maintenance due to the frequent wear and tear on the belt drives. To our knowledge, only one commercialized device claimed to solve these reported issues using a backdrivable linear actuated mechanism, but with minimum information revealed [6], [7]. The current paper explores an alternative system architecture with a non-backdrivable mechanism, and attempts to provide explicit evidence of the potential benefits.

End-effector upper limb rehabilitation devices typically offer three training functions tailored to specific rehabilitation interventions: robot-guided trajectory following, human-guided trajectory following, and free-moving. These training functionalities aim to map the sequential stages of conventional physical therapy progression [13], [18], [19]. The robot-guided trajectory following function is primarily utilized in the early stages of rehabilitation for stretching and passive range of motion (ROM) exercises [20]. Patients follow a predetermined 2D trajectory operated by the device, without using strength or exerting forces. The human-guided trajectory following function attempts to facilitate active range of motion (ROM) exercises and resistance training [20], [21]. In this function, the device provides assistance or resistance as needed. The free-moving function allows users unrestricted movement within the 2D workspace, facilitating engagement with rehabilitation games, promoting sensorimotor training, and enhancing tactile feedback, motor planning, and sensory and proprioceptive awareness [22].

B. Novel Contributions

This paper introduced the Gantry Arm Rehabilitation Device (GARD), a low-cost, easily maintainable end-effector-based upper limb rehabilitation robot, as shown in Fig. 2. The proposed design for GARD featured a non-backdrivable mechanism where previous research rarely delved into. The design incorporates two ball-screw-driven linear actuators for the x and y axis. Compared to conventional multi-link robots, the proposed robot offers better stability along the z-axis. Compared to the pulley-belt driven robots, the proposed system exhibits enhanced wear resistance, owing to its ball-screw direct drive mechanism. The proposed control method based on non-backdrivable design uniquely offers functionalities such as Range of Motion (ROM) restricted moving and hard boundary human-guided trajectory following, in addition to providing all functionalities of existing commercial devices with superior performance. Three main challenges are addressed in this paper.

First, a virtual dynamics model is required for controlling a non-backdrivable mechanism with sensor force as input and end-effector velocity as output. We proposed an admittance control method to emulate a virtual mass, static resistance, and speed damper, which achieves natural sensation of free moving.

Second, implementing end-effector area restriction control on a non-backdrivable mechanism using motor velocity control presents the challenge of position error accumulation. This

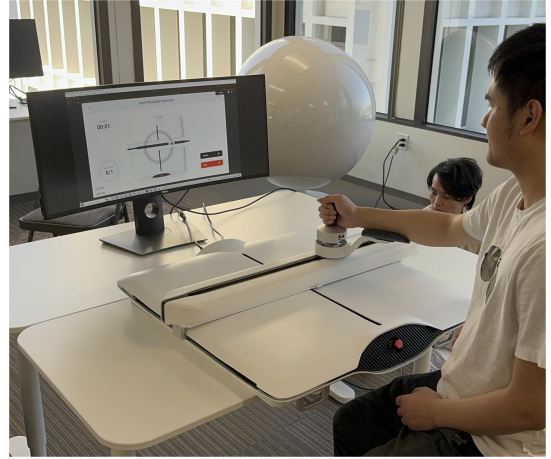


Fig. 2. The Gantry Arm Rehabilitation Device (GARD) operates in Human-guided Trajectory Mode along a circular trajectory. The GARD can provide either assistance or resistance to support physical therapy training.

error arises from both the control discretization and the motor acceleration limitations. While increasing the control frequency and using higher quality motors can reduce the error, it cannot be entirely eliminated and tends to accumulate over time. We proposed a novel Implicit Euler Velocity Control (IEVC) algorithm which can completely and efficiently address this problem.

Third, trajectory tracking necessitates customization for individual users. No prior research has proposed a generalized method capable of controlling along any given trajectory. Existing studies [5], [17] or commercial products [7] focus on trajectory with symbolic solutions. Our proposal introduces a numerical solution to provide force assistance or resistance along any trajectory, including hand-drawn ones. This method entails computer vision inspired numerical trajectory gradient generation to determine the direction of force assistance or resistance, coupled with a series of admittance and impedance controls on the end-effector [23].

II. GANTRY ARM REHABILITATION DEVICE

A. Mechanical Design

The Gantry Arm Rehabilitation Device (GARD) end-effector offers a flexible range of motion within a 65x55cm 2D workspace. This device utilizes two rotary actuators coupled with ball screws, enabling linear movement along the x and y axis, as depicted in Fig. 3. The ball screws operate at a ratio of 1 turn to 2 millimeters. The actuators can achieve a maximum speed of 80 revolutions per second, with acceleration limited to 800 revolutions per second squared. Additionally, each actuator provides a maximum torque output of 0.22Nm.

B. Electrical Design

The power source is a medical-grade power supply with a rated output of 24V and 6.5A. This power is distributed via a power distribution board to various components including the motor controller, force sensor, and controller board. Two motor controllers are incorporated to connect with two Brushless DC motors equipped with 1000CPR resolution optical encoders for

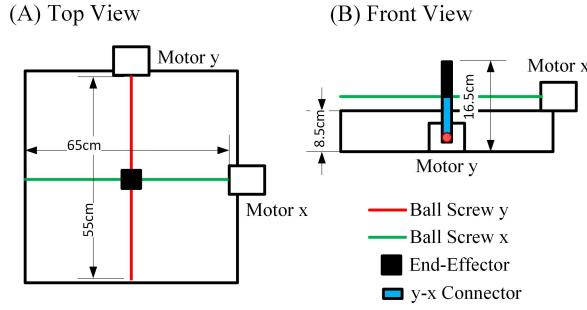


Fig. 3. Mechanical design of GARD. (A) The top view illustrates the 65x55cm 2D workspace attained through the use of two rotary actuators and ball screws. (B) The front view showcases the y-axis actuator and ball screw, which can move both the end-effector and the x-axis actuator with the ball screw in the y-direction. The x-axis actuator moves the end-effector in the x-direction.

precise control over the x and y axis ball screws. Additionally, the system employs two limit switches for motor-homing purposes. For force sensing at the end-effector, a low-cost Galoce GPB160 3-axis load cell is employed, utilizing an ADS1232 SPI ADC converter. To manage low-level control and communication with the high-level controller, the limit switches, ADC converters, and motor drivers are all interfaced with an STM32 microcontroller unit (MCU).

C. Control Hierarchy

The GARD features a two-level control hierarchy comprising a High-level Virtual Dynamic Model and a Low-level Firmware Controller, as depicted in Fig. 4. At the high level, the Virtual Dynamic Model computes the desired motor velocity based on sensor data and user settings. At the low level, the Firmware Controller manages sensor data collection, timing regulation, and motor control.

The current structural setup diverges from conventional admittance control systems. Unlike conventional systems, where the virtual dynamic model and motor control are not separated due to the influence of applied forces on robot dynamics, both input force and desired velocity must be considered in motor torque calculations. However, the proposed device GARD features a non-backdrivable end-effector, where user force does not influence end-effector motion, allowing the separation of dynamic model and motor control. The proposed structure enables us to establish a clear control hierarchy, and maximize the integration advantages of commercial motor controllers, that is, the integrated commercial motor controller firmware dedicated to motor velocity control typically operates at much higher control frequencies, and is more stable and efficient than user's implementation on a multitask MCU.

III. GARD OPERATION MODES

Three distinct operation modes have been implemented to support patients at different stages of recovery: Robot-guided Trajectory Mode, Free Mode, and Human-guided Trajectory mode. Additionally, a Graphical User Interface (GUI) is provided for all operational modes, offering GUI functionality and rehabilitation gaming features. This section will introduce these operation modes and the corresponding control algorithm used.

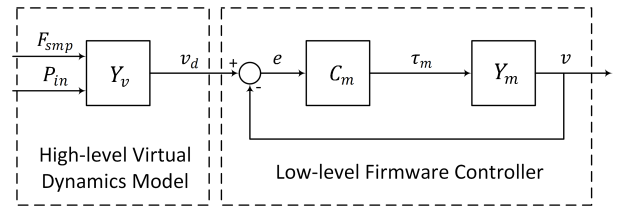


Fig. 4. Control hierarchy of GARD. The high-level Virtual Dynamics Model computes the desired motor velocity based on sensor data and user settings. The Low-level Firmware Controller manages sensor data collection, timing regulation, and motor control. F_{smp} denotes data from the force sensor. P_{in} denotes the current position of the end-effector. Y_v denotes the virtual dynamics. v_d denotes the desired velocity. C_m denotes the motor controller. Y_m denotes the robot dynamics.

Control Block Diagram for Robot-guided Trajectory Mode

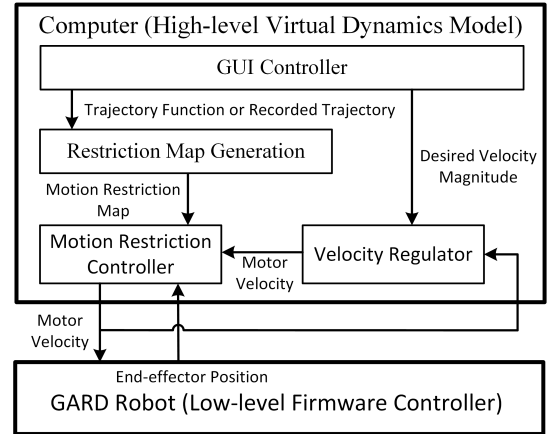


Fig. 5. Control hierarchy for Robot-guided Trajectory Mode. The core control block in Robot-guided Trajectory Mode is the Motion Restriction Controller which takes a Motion Restriction Map and a velocity as input. The GUI Controller provides the Motion Restriction Map, which specifies the permitted end-effector positions. The Velocity Regulator provides a regulated velocity based on the user's desired speed and the previous motor velocity direction. The Motion Restriction Controller will limit the end-effector's motion inside the permitted area by modifying the input velocity using the IEVC algorithm. The output velocity of the Motion Restriction Controller will be sent to the Low-level Firmware Controller.

A. Robot-guided Trajectory Mode

Designed to enable passive rehabilitation training for the patient's arm, Robot-guided Trajectory Mode entails the robot automatically following a pre-set trajectory at a user-defined speed. In this non-interactive mode, exerted force on the end-effector does not influence the robot's motion. It's typically employed during the early recovery stage when external force guidance is required for completing arm movements.

The Robot-guided Trajectory Mode control hierarchy is shown in Fig. 5. The GUI controller in robot-guided mode provides desired moving speed and Motion Restriction Map. It then passes the map to the Motion Restriction Controller. The Velocity Regulator provides a regulated velocity based on the user's desired speed and the previous motor velocity. The Motion Restriction Controller will limit the end-effector's motion inside the permitted area by modifying the input velocity using the IEVC algorithm. The Motion Restriction Controller and IEVC algorithm are reused in all modes, details can be found in Sec. IV-A.

Control Block Diagram for Free Mode & Human-guided Trajectory Mode with Hard Boundary

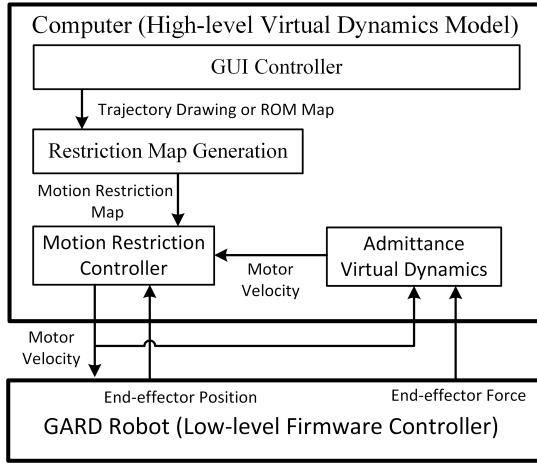


Fig. 6. Control hierarchy for Free Mode and Human-guided Trajectory Mode with hard boundary. The GUI controller generates Motion Restriction Map base on the user's ROM restrictions and pass the map to the Motion Restriction Controller. The Admittance Virtual Dynamics block simulates a mass-friction-damper system and outputs the calculated motor velocity to the Motion Restriction Controller.

Control Block Diagram for Human-guided Trajectory Mode with Soft Boundary

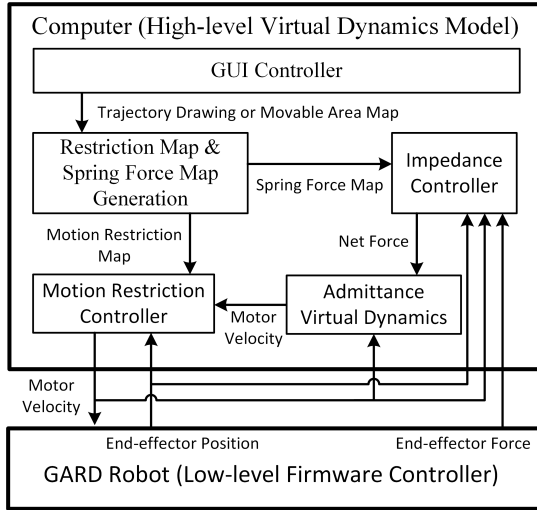


Fig. 7. Control hierarchy for Human-guided Trajectory Mode. In addition to the Motion Restriction Map, the GUI controller also generates the Spring Force Map used by the Impedance Controller. The Impedance Controller calculates the net force of the end-effector input and the impedance spring-damper system, pass the result to the admittance virtual dynamics. The rest of the control blocks are identical to Free Mode.

B. Free Mode

The Free Mode is an interactive mode, which can be used in a later recovery stage to facilitate participation in rehabilitation games and promote sensorimotor training. The Free Mode allows the user to move the end-effector within the user's Range of Motion (ROM). ROM is defined as the area bounded by a closed trajectory traversed by the end-effector. An example of the generation of ROM Restriction Map is illustrated in Fig. 13 (A) and (B). The interaction with the ROM boundary resembles encountering a hard, smooth wall-

like boundary, restricting the user's arm motion inside a safe workspace to avoid injuries.

Fig. 6 presents the control hierarchy for the Free Mode. This mode contains two key control blocks. The first control block is the Motion Restriction Controller, which is identical to the block in Robot-guided Trajectory Mode. The second control block is the Admittance Virtual Dynamics block, which involves implementing virtual robot dynamics where the robot simulates the behavior of a mass-friction-damper system (detailed shown in Sec. IV-B). The Admittance Virtual Dynamics block takes net external force as input on body and sends the desired velocity to the Motion Restriction Controller. The combination of the Motion Restriction Controller and the Admittance Virtual Dynamics enables the end-effector to move freely inside the permitted area, and interact with a hard, smooth wall-like area boundary.

C. Human-guided Trajectory Modes

The Human-guided Trajectory Modes are utilized for both active Range of Motion (ROM) training and resistance training. The proposed device comprises two submodes: the Human-guided Trajectory Mode with hard boundary and the Human-guided Trajectory Mode with soft boundary, offering varying degrees of freedom for active ROM training.

In Human-guided Trajectory Mode with hard boundary, users can maneuver the end-effector freely along a trajectory with hard boundaries. The control structure of this mode mirrors that of the Free Mode, because under our proposed method the trajectory restriction and the area restriction are identical. The method used to generate Motion Restriction Map is listed in Sec. IV-A.

Conversely, the Human-guided Trajectory Mode with soft boundary permits greater flexibility in rehabilitation training. Here, users can guide the end-effector along a trajectory with soft boundaries, allowing deviations from the desired path. Automatic assistance force is applied to realign the end-effector with the trajectory when necessary. The control hierarchy of the Human-guided Trajectory Mode with soft boundary is outlined in Fig. 7. This mode incorporates three primary control blocks. In addition to the Motion Restriction Controller and Admittance Virtual Dynamics used in previous modes, an Impedance Controller block is introduced. This block use impedance control to provide the assistance force for trajectory realignment. This control block will adjust the end-effector force based on the Impedance Force Map and end-effector position, sending the modified net force to the Admittance Virtual Dynamics for further computation. The detail of Spring Force Map generation and Impedance Controller can be found in Sec. IV-C.

IV. CONTROL ALGORITHMS

This section introduces the control algorithms used for GARD to enable different operation modes. Sec. IV-A describes the algorithm used for motion restriction and trajectory following. Sec. IV-B describes the algorithms that allow the end-effector to move with simulated virtual dynamics. Sec. IV-C describes the algorithms that add a soft boundary to the Human-guided Trajectory Mode.

A. Motion Restriction Algorithms

A common practice in implementing the trajectory-following algorithm using velocity control is to decompose the current velocity into tangential and radial velocity, and adjust them accordingly. However, these types of algorithms share a common issue such that the trajectory following error can accumulate over time resulting in increased deviation. Take circular trajectory as an example, a trivial way to limit the end-effector movement on a circular trace is to dynamically calculate the tangential direction at current position and marching only in that direction. However, with this method in practice, the error caused by the control discretization and the motor acceleration limitations will accumulate and will cause the end-effector to move further away over time. This example of truncation error accumulation is the same as the local truncation error accumulation in solving the initial value problems using the Explicit Euler Integral [24]. We proposed the Implicit Euler velocity control (IEVC) algorithm initially for solving this error accumulation issue in free moving along an arbitrary trajectory restriction. However, we discover that this algorithm can be naturally extended to 2D area restriction or even 3D space restriction. Hence, we define the **Motion Restriction Control** as the end-effector moving control under a virtual positional restriction. Areas in which the end-effector is allowed to move freely are defined as the **permitted area**, otherwise are defined **prohibited area**.

The proposed IEVC algorithm can effectively restrict the end-effector inside any permitted area, implemented in Fig. 5 as Motion Restriction Controller block. This algorithm enables the end-effector to move freely inside the permitted area and interact with a hard-smooth-wall like area boundary. The core of this algorithm is dynamically searching and choosing the best chasing target. To make the algorithm generalizable to any scenario, it is implemented upon a discretized taskspace with $W_g \times H_g$ positions, and use a 2D matrix of equal size to represent the taskspace motion restriction which referred to as the Motion Restriction Map. The detailed Motion Restriction Map generation method and IEVC algorithm are described in the following two subsections.

1) *Motion Restriction Map Generation*: The task space of GARD is discretized into $W_g \times H_g$ positions, generating a 2D matrix of equal size referred to as the Motion Restriction Map \mathbf{M}_{rs} . The \mathbf{M}_{rs} can be viewed as a grayscale image. Each pixel entry on \mathbf{M}_{rs} corresponds to a physical GARD end-effector location. A pixel storing a value of 0 indicates that the corresponding location is the **prohibited area**; otherwise, the location is the **permitted area**. \mathbf{M}_{rs} will be initialized with all 0, meaning all prohibited area.

For an trajectory restriction defined using implicit functions $f(x, y) = 0$ or more generalized area restriction defined using $\mathbf{F}(x, y) < \mathbf{0}$, \mathbf{M}_{rs} can be generated by iterating through all entries $[i, j]$ on \mathbf{M}_{rs} and evaluating $\text{abs}(f(j, i)) < E_s$ or $\mathbf{F}(j, i) < \mathbf{0}$. E_s is the trajectory width for trajectory restriction. If $[i, j]$ satisfy the function, $\mathbf{M}_{rs}[i, j]$ will be assigned 1, which represents the permitted area.

For other general user-defined motion restrictions such as a hand-drawn trajectory restriction, \mathbf{M}_{rs} can also be generated

or edited using an image editing tools.

2) *Motion Restriction Controller (IEVC algorithm)*: The IEVC algorithm takes the current velocity \mathbf{V}_{in} , current position \mathbf{P}_{in} and the Motion Restriction Map \mathbf{M}_{rs} as input, and will output the motion restricted end-effector velocity \mathbf{V}_r which is guaranteed to limit the end-effector position towards the permitted area.

The key concept of this algorithm is to predict end-effector location in the next step and adjust the current velocity output, inspired by the Implicit Euler Method in solving the initial value problem [24]. The algorithm will first draw a circle centered at the end-effector \mathbf{P}_{in} with radius proportional to the current speed magnitude. The proportional gain G_v needs to be adjusted by the transmission ratio between the motor velocity and the end-effector velocity. Then, the algorithm will mark all circle's intersection points with the permitted area as candidate points for the next chasing target. An array of normalized vectors is generated by pointing the current end-effector position to all candidate points. Next, the algorithm will iterate through the generated vector array, and find the vector that has the most aligned direction with the input end-effector velocity (\mathbf{V}_{in}). The most aligned vector in the vector array is chosen as the end-effector final direction vector \mathbf{D}_{next} . Finally, the end-effector output velocity \mathbf{V}_r is calculated by combining the direction of \mathbf{D}_{next} with the non-zero clipped magnitude of \mathbf{V}_{in} 's projection onto the \mathbf{D}_{next} .

Fig. 8 illustrates an example of IEVC output calculation. This example also shows that even when current position \mathbf{P}_{in} does not lie inside the permitted area (trajectory), the IEVC can still effectively restrict the end-effector location on the area boundary by exponentially minimizing the divergence distance over time steps. Algo. 1 present the sudo code for IEVC.

The helper functions implementation of IEVC can be found in Algo. 4. The *circleMap()* function generates a points-on-the-circle list which contains all positions on the taskspace that has the distance equal to R_{circle} within a tolerance. The resultant list will be provided to *findIntersec()* function to find all IEVC candidate points.

B. Admittance Virtual Dynamics

Admittance Virtual Dynamics block is used in both Free mode and Human-guided Trajectory Modes. The goal of this control block is to simulate an adjustable mass-friction-damper dynamics allowing natural motion of the end-effector.

Given a simulated mass, we have the following equation of motion in the Laplace domain:

$$\begin{aligned} f &= s m_v v k_r \\ \frac{v}{f} &= \frac{1}{m_v k_r} \cdot \frac{1}{s} \end{aligned} \quad (1)$$

where, m_v denotes the virtual mass. k_r denotes the transmission ratio between the motor to end-effector velocity. T_s denotes the time step size.

The Laplacian domain model cannot be directly used for discrete control. There are two steps to convert the Laplacian

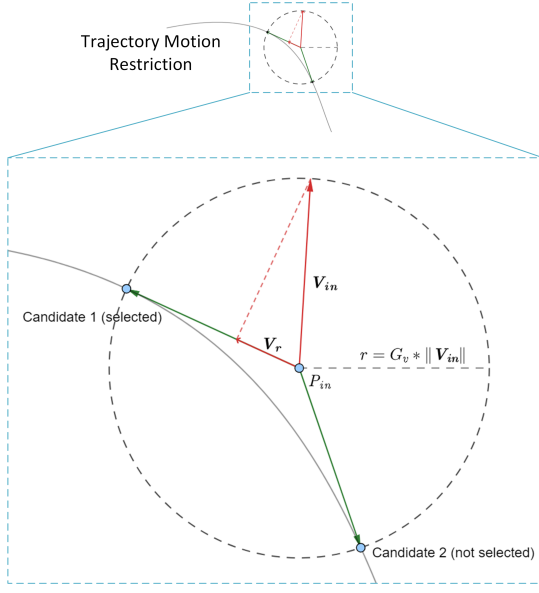


Fig. 8. Illustration for IIEVC calculation at position P_{in} with velocity V_{in} . In this example, the IIEVC finds 2 candidates according to the intersection circle centered at P_{in} with radius $G_v * \|V_{in}\|$. Candidate 1 is selected due to higher directional alignment with V_{in} . The output V_r is P_{in} 's projection onto candidate 1's direction. The IIEVC is stable because the restricted velocity given by IIEVC always target towards permitted area. In the example above, even when current position P_{in} does not lie inside the permitted area (trajectory), the error will decay exponentially over time steps and IIEVC can still effectively restrict the end-effector location on the area boundary.

Algorithm 1 Implicit Euler velocity control (IIEVC)

Input: P_{in} , V_{in} , M_{rs} , G_v

Output: V_r

```

1:  $R_{circle} \leftarrow \text{round}(G_v * \text{norm}(V_{in}))$ 
2:  $\text{candidatesList} \leftarrow \text{findIntersec}(M_{rs}, R_{circle}, P_{in})$ 
3: if  $\text{length}(\text{candidatesList}) > 0$  then
4:    $D_{next} \leftarrow \text{None}$ 
5:    $\text{maxProj} \leftarrow -\infty$ 
6:   for all  $P_c$  in  $\text{candidatesList}$  do
7:      $D_c \leftarrow \text{normalize}(P_c - P_{in})$ 
8:      $\text{curProj} \leftarrow (V_{in} \cdot D_c)$ 
9:     if  $\text{curProj} > \text{maxProj}$  then
10:       $\text{maxProj} \leftarrow \text{curProj}$ 
11:       $D_{next} \leftarrow D_c$ 
12:     end if
13:   end for
14:    $V_r \leftarrow \text{max}(\text{maxProj}, 0) * D_{next}$ 
15:   return  $V_r$ 
16: end if

```

domain model into discrete control. First, take the Z-transform with Tustin estimator:

$$\begin{aligned} \frac{v}{f} &= \frac{1}{m_v k_r} \cdot \frac{T_s z + 1}{2z - 1} \\ \Rightarrow v &= \frac{T_s}{m_v k_r} \cdot \frac{f + z^{-1}f}{2} + z^{-1}v \end{aligned} \quad (2)$$

Second, transform the z-domain result back to the time domain to generate discrete control implementation:

$$v_k = \frac{T_s}{m_v k_r} \cdot \frac{f + f_{k-1}}{2} + v_{k-1} \quad (3)$$

Algo. 2 shows the implementation of Eq. 3. The algorithm takes current input force F_{in} , input force on last time step F_{last} , velocity on last time step V_{last} , virtual mass m_v , damping ratio ζ_a , and friction coefficient μ as input, and will output the desired velocity V_d . The V_d will be sent to the Motion Restriction Controller. The motor velocity from the Motion Restriction Controller will be sent to low level GARD firmware (e.g. MCU, motor controller) for close loop velocity control.

Algorithm 2 Admittance Virtual Dynamics

Input: F_{in} , F_{last} , V_{last} , ζ_a , m_v , μ

Output: V_d

```

1:  $Y_m \leftarrow T_s / m_v / k_r$ 
2:  $V_{last} \leftarrow V_{last} * (1 - \zeta_a * Y_m)$ 
3:  $V_d \leftarrow V_{last} + (F_{in} + F_{last}) / 2 * Y_m$ 
4:  $V_d \leftarrow \text{max}(\mathbf{0}, V_d - m_v * 9.8 * \mu * Y_m)$ 
5: return  $V_d$ 

```

C. Impedance Controller

Impedance controller is used together with Admittance Virtual Dynamics in the Human-guided Trajectory Mode with soft boundary to simulate a permitted area with spring-damper (impedance) boundary.

The Impedance Controller outputs the net external forces to the Admittance Virtual Dynamics control block. The output force from the Impedance Controller is a compositional force of the force applied at the end-effector, the simulated impedance spring force (referred to as impedance spring force hereafter), and the simulated impedance damper force (referred to as impedance damper force hereafter). The impedance spring force and the impedance damper force are computed using a precalculated Spring Force Map. The detail of the impedance force calculation is described below.

We proposed an impedance force calculation algorithm that can automatically calculate the impedance force at any taskspace position on any given Motion Restriction Map. It is done using a precalculated 2D Spring Force Map which will provide all information needed for the impedance force calculation. The Spring Force Map is generated using M_{rs} and 2D convolution.

To demonstrate why convolution is needed, consider a simplified impedance force calculation problem in 1D. As illustrated in Fig. 9, $M_{rs}(x)$ is our example 1D Motion Restriction Map. Each x value corresponds to a end-effector location on the x axis, meaning all positions between $2 \leq x \leq 6$ are permitted area. $\text{Kernel}_{sw}(x)$ is a unit impulse function that equals to 1 between $-0.5 \leq x \leq 0.5$ which is used as the convolution kernel. Note that in Fig. 9 (C), the convolution result between $M_{rs}(x)$ and the $\text{Kernel}_{sw}(x)$ shows a straight transaction around the permitted area boundary same as the ideal characteristic curves of a spring.

Therefore, in our simplified 1D example, we can define the Spring Force Map F_{spr} as a mapping function which $F_{spr}(x)$ will give the magnitude of the impedance spring force at position x . The Spring Force Map can be calculated using

1-flipped convolution result between the Motion Restriction Map $M_{rs}(x)$ and the impulse convolution kernel:

$$F_{spr}(x) = K_{sp}L_{max}(1 - M_{rs}(x) \otimes Kernel_{sw}(x)) \quad (4)$$

where K_{sp} denotes the spring stiffness and L_{max} denotes the width of the impedance force zone that can be controlled by the width of the impulse kernel $Kernel_{sw}(x)$. The direction of the impedance spring force can also be computed by the sign of the negative local derivative:

$$F_{dir} = sgn\left(-\frac{\partial F_{spr}}{\partial x}\right) \quad (5)$$

The impedance damper force can be calculated using the direction of the impedance spring force and the current end-effector velocity.

The same concept can be generalized into 2D space. The 2D Spring Force Map for any given trajectory or ROM can be generated using a 2D convolution between the Motion Restriction Map M_{rs} and a 2D uniformly filled circular kernel. The impedance spring force direction can be computed by the negative local gradient direction of the Spring Force Map at the current end-effector position. The width of the impedance force zone can be controlled by the diameter of the circular kernel. Fig. 10 illustrates an example spring force vector map calculation process for a hand-drawn restriction map. The first step is to expand the trajectory in the radial direction. The reason for expansion can be observed in Fig. 9 (B) and Fig. 9 (C). In Fig. 9 (B), the permitted area boundaries are at $x = 2$ and $x = 6$, but in Fig. 9 (C) the generated impedance force zone is between $1.5 \leq x \leq 2.5$ and $5.5 \leq x \leq 6.5$. The generated impedance force zone will be centered at the original boundary location with a width equal to the diameter of the convolution kernel. Therefore, the permitted area (trajectory) needs to be expanded in the radial direction by the radius of the convolution kernel to create space for the impedance force zone. The expansion can be achieved through convolution using the same 2D uniformly filled circular kernel, followed by thresholding the resultant output (setting x to 1 if $x > 0$, otherwise to 0 for all x in $(M_{rs} \otimes Kernel_{cir})$). Fig. 10 (B) shows the resulting expanded Motion Restriction Map using a 6 mm radius uniformly filled circular kernel. Fig. 10 (C) shows the generated Spring Force Map with a 12 mm impedance zone along the trajectory. Fig. 10 (D) shows the derived spring force vector field using the proposed impedance force calculation algorithm and the Spring Force Map.

Algo. 3 shows the implementation of the Impedance Controller. It takes the input force F_{in} , the velocity on last time step V_{last} , the current position P_{in} , the precalculated Spring Force Map F_{spr} , the spring stiffness K_{sp} , and the damping ratio ζ_i as input. And output the compositional force F_o .

V. EXPERIMENTS

The experiments are performed in three parts. First, the complexity analysis of the proposed high-level control. Second, the performance assessment of GARD's different operation modes and control blocks. Third, comparison to the state-of-the-art end-effector upper limb rehabilitation devices.

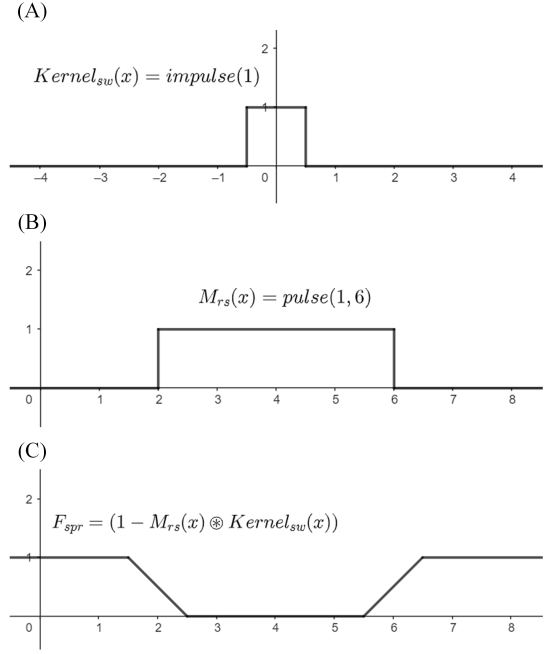


Fig. 9. Example of 1D Spring Force Map calculation using convolution. (A) The 1D impulse kernel $Kernel_{sw}(x)$. (B) The 1D Motion Restriction Map $M_{rs}(x)$. Each x value corresponds to an end-effector location on the x axis. All positions between $2 \leq x \leq 6$ are permitted area. (C) Spring Force Map F_{spr} calculated using 1-flipped convolution result $(1 - M_{rs}(x) \otimes Kernel_{sw}(x))$. The convolution between $M_{rs}(x)$ and the $Kernel_{sw}(x)$ shows a nice straight transaction around the boundary same as the characteristic curves of a spring. Width of the transaction area equals width of the impulse kernel.

Algorithm 3 Impedance Controller

Input: F_{in} , V_{last} , P_{in} , F_{spr} , K_{sp} , ζ_i ,

Output: F_o

- 1: $[P_x, P_y] \leftarrow P_{in}$
- 2: $F_{dx} \leftarrow F_{spr}[P_y, P_x + 1] - F_{spr}[P_y, P_x - 1]$
- 3: $F_{dy} \leftarrow F_{spr}[P_y + 1, P_x] - F_{spr}[P_y - 1, P_x]$
- 4: $F_{dir} \leftarrow normalize(-[F_{dx}, F_{dy}])$
- 5: $F_o \leftarrow F_{in} + K_{sp} * F_{spr}[P_{in}] * F_{dir}$
- 6: $F_o \leftarrow F_o + \zeta_i * (V_{last} \cdot F_{dir}) * F_{dir}$
- 7: **return** F_o

A. Control Algorithms Complexity Analysis

The complexity analysis of the proposed control algorithms is conducted concerning the taskspace discretization precision ($n \times n$ taskspace discretization). The results are displayed in Tab. I. The proposed control algorithms consider $O(n)$ overall runtime time complexity and $O(n^2)$ overall space complexity.

The proposed algorithm is efficient for several reasons. First, a runtime time complexity of $O(n)$ is affordable for any modern PC or MCU. Although the generation of the circle map ($circleMap(R_{circle})$ in helper functions) can have a time complexity of $O(n^2)$, since R_{circle} is always an integer and motors have physical maximum speed limits, precalculating all points-on-the-circle lists for all possible R_{circle} values is feasible, and will therefore not affect the runtime performance. Second, adding trajectories, permitted areas, and obstacles incurs **zero** run time performance cost. Designers can create

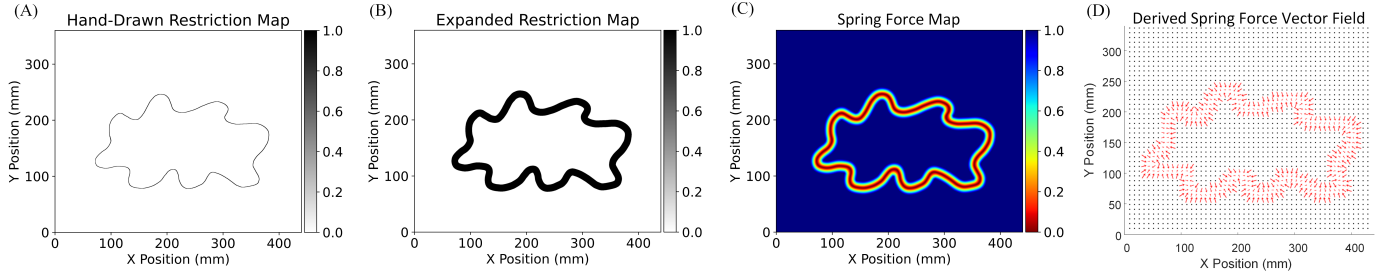


Fig. 10. Example of impedance force calculation for a hand-drawn Motion Restriction Map. (A) The original hand-drawn Motion Restriction Map. (B) The Motion Restriction Map expanded using a 6 mm radius uniformly filled circular kernel. (C) The generated Spring Force Map with a 12 mm impedance force zone along the trajectory. (D) The derived spring force vector field using the proposed impedance force calculation algorithm and the Spring Force Map.

Motion Restriction Maps for games and applications without concern any runtime performance impact. Third, the proposed Human-guided Trajectory Mode with soft boundary (the most complicated one), implemented with C#, under 2200×1700 taskspace discretization costs an average time step of $10\mu s$ when running on i7-8750H. This indicates that solving the 2D constraint control problem on modern CPUs using the proposed algorithm has significant computational surplus. Furthermore, the algorithm's high degree of parallelizability underscores its potential for further runtime optimization, suggesting its substantial potential for real-time 3D taskspace motion restriction control.

TABLE I
ALGORITHM COMPLEXITY WITH RESPECT TO TASKSPACE
DISCRETIZATION ACCURACY.

Function	Space Complexity	Time Complexity (runtime)
Motion Restriction Map Generation	$O(n^2)$	N/A
IEVC circleMap	$O(n)$	N/A
IEVC findIntersec	$O(n)$	$O(n)$
IEVC Choose candidate	$O(n)$	$O(n)$
IEVC overall	$O(n^2)$	$O(n)$
Admittance Virtual Dynamics	$O(1)$	$O(1)$
Spring Force Map Generation	$O(n^2)$	N/A
Impedance Controller	$O(1)$	$O(1)$
Adding Trajectories	0	0
Adding Permitted Areas	0	0
Adding Prohibited Areas	0	0
Proposed method overall	$O(n^2)$	$O(n)$

B. Experimental Validation of Robot-Guided Trajectory Mode

One of the primary functionality of rehabilitation robot revolves around trajectory tracking. Employing a non-backdrivable end-effector allows us to strictly follow the desired trajectory without being affected by external forces in the Robot-guided Trajectory Mode. Fig. 11 shows the trajectory following test result of the Robot-guided Trajectory Mode. One healthy subject executed robot-guided trajectory following mode on two function-based and two hand-drawn trajectories, both the desired end-effector positions and measured end-effector positions are recorded and plotted. The error is calculated by measuring the closest distance to permitted area for each recorded end-effector position. The average Mean

Algorithm 4 IEVC Helper functions implementation

```

1: procedure inCircle( $x, y, lineWidth$ )
2:   return  $abs(x^2 + y^2 - 1) < lineWidth$ 
3: end procedure
4: procedure circleMap( $R_{circle}$ ):
5:    $mapLen \leftarrow R_{circle} * 2 + 10$ 
6:    $M_{cir} \leftarrow emptyList()$ 
7:   for all  $[x, y]$  in  $M_{cir}$  do
8:      $dx \leftarrow x - R_{circle} - 5$ 
9:      $dy \leftarrow y - R_{circle} - 5$ 
10:     $ndx \leftarrow dx / R_{circle}$ 
11:     $ndy \leftarrow dy / R_{circle}$ 
12:     $wLine \leftarrow 2 / R_{circle}$ 
13:    if inCircle( $ndx, ndy, wLine$ ) then
14:       $M_{cir}.append([dx, dy])$ 
15:    end if
16:  end for
17:  return  $M_{cir}$ 
18: end procedure
19: procedure findIntersec( $M_{rs}, R_{circle}, P_{in}$ )
20:   $[P_x, P_y] \leftarrow P_{in}$ 
21:   $M_{cir} \leftarrow circleMap(R_{circle})$ 
22:   $candidatesList \leftarrow emptyList()$ 
23:  for all  $[dx, dy]$  in  $M_{cir}$  do
24:    if  $M_{rs}[P_y + dy, P_x + dx] > 0$  then
25:       $P_c \leftarrow [P_x + dx, P_y + dy]$ 
26:       $candidatesList.append(P_c)$ 
27:    end if
28:  end for
29:  return  $candidatesList$ 
30: end procedure

```

Absolute Error (MAE) of four trials between the intended and recorded end-effector positions stands at $0.012mm$.

C. Experimental Validation of Free Mode

The Free Mode has two primary functionalities. First, it incorporates an Admittance Virtual Dynamics control block, which emulates the non-backdrivable end-effector as a free mass in the real world. Second, it enables free moving with the ROM restriction. Two experiments are performed to verify these two functionalities accordingly.

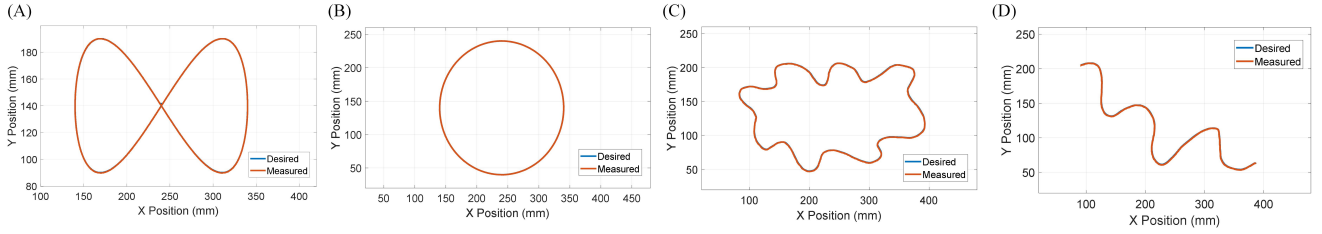


Fig. 11. Desired and measured end-effector position and error analysis in Robot-guided Trajectory Mode. One healthy subject operate Robot-guided Trajectory Mode on two function-based and two hand-drawn trajectories, the desired end-effector positions and measured end-effector positions are recorded and plotted on figures. The error is calculated by measuring the closest distance to permitted area for each recorded end-effector position if the end-effector is outside the permitted area. (A) Infinite shaped trajectory calculated using equation: $x^4 - x^2 + y^2 = 0$. The Mean Absolute Error (MAE) between desired and measured is $0.00823mm$. (B) Circle shaped trajectory calculated using equation: $x^2 + y^2 - 25^2 = 0$. The MAE between desired and measured is $0.023mm$. (C) Hand drawn circular trajectory. The MAE between desired and measured is $0.00878mm$. (D) hand drawn line trajectory. The MAE between desired and measured is $0.00763mm$.

The performance of the Admittance Virtual Dynamics simulation is the key for achieving smooth and natural moving end-effector in both Free Mode and Human-guided Trajectory Mode. Fig. 12 (A) and (B) depict six trials of circular motion performed using Free Mode by a healthy subject, simulating objects with masses of 5, 10, 15, 20, 25, and 30 kilograms, moving freely on a plane with no motion restriction, bearing with a friction coefficient of 0.02. The user, a healthy subject, is instructed to follow an approximately circular trajectory. In Fig. 12 (C), the desired and measured velocities of the end-effector, simulating an object with a mass of 30 kilograms, are demonstrated. The overall outcomes are summarized in Tab. II. The results indicate that the Admittance Virtual Dynamics block can accurately simulate objects with masses of 10 kilograms to 30 kilograms. However, when simulating objects with 5 kilograms or lower masses, the end-effector experiences larger velocity error due to motor acceleration limit.

The range of motion (ROM) is defined as the area bounded by a closed trajectory traversed by the end-effector. The ROM Motion Restriction Map is generated by filling all triangles constructed by the starting point and two consecutive positions of the end-effector. Fig. 13 (A) and (B) demonstrate the generation of a Motion Restriction Map. The trajectory recorded in (A) is used to generate the Motion Restriction Map in (B). Additionally, Fig. 13 (C) and (D) provide an illustration of an experiment using the Free Mode with Motion Restriction Map generated in (B). In Fig. 13 (C), the end-effector trajectory is shown, this experiment contains both movement inside the permitted area and movement interacting with the area boundary. The end-effector can move freely inside the permitted area and interact with a hard, smooth, wall-like boundary. Fig. 13 (D) highlights instances at points A, B, and C where dedicated forces are applied trying to exceed the ROM restriction, yet the end-effector remains within the ROM.

D. Experimental Validation of Human-guided Trajectory Modes

The Human-guided Trajectory Mode comprises two sub-modes: Human-guided Trajectory Mode with hard boundary and Human-guided Trajectory Mode with soft boundary. In Human-guided Trajectory Mode with hard boundary, the user can move the end-effector along a trajectory with a smooth

hard boundary, sharing the same control method as the Free Mode. In Human-guided Trajectory Mode with soft boundary, the user can move the end-effector along a trajectory with a soft (impedance force) boundary, which will provide assistance force pulling the end-effector back towards the trajectory when the position deviate from the trajectory. Two key functionalities of the Human-guided Modes are highlighted. The first functionality involves the motion restriction algorithms applied to the trajectory to ensure the user can only move the end-effector along the designed trajectory. The second functionality entails impedance control, creating a soft boundary on the trajectory, simulating a impedance spring damper force towards trajectory. Two experiments are conducted to verify the key functionalities of the Human-guided Mode.

The first experiment aims to validate the performance of the IEVC on motion restricted control. A healthy subject is asked to move the end-effector and complete one circular motion for each trial. During each trial, a Motion Restriction Map which only allow the end-effector to move on a thin trajectory is loaded to the Motion Restriction Controller, and a certain level of random noise is injected on the load cell during motion to simulate undesired force which can possibly affect the end-effector motion. Fig. 14 depicts a total of six trials of human-guided trajectory following on two different trajectory shapes under three different levels of random force injected into the end-effector as noise. The result shows that in all trials, the recorded trajectory almost completely overlaps with the Motion Restriction Map, indicating that the proposed control method effectively restricts the end-effector motion on the trajectory. Tab. III presents the quantitative MAE of each trial. The error is calculated by measuring the closest distance to the permitted area for each recorded end-effector position if the end-effector is outside the permitted area. Interestingly, the error decreases under higher noise levels. This is because the error of the proposed control algorithm depends only on the moving speed and the trajectory. A large injection noise makes it difficult for the subject to move the end-effector, thus reducing the error. The results of this experiment demonstrate that the IEVC algorithm can effectively restrict the end-effector motion within any permitted area, making it an ideal choice for the motion restriction controller.

The second experiment involves free moving inside an impedance force zone with radius of 14 cm. The Spring

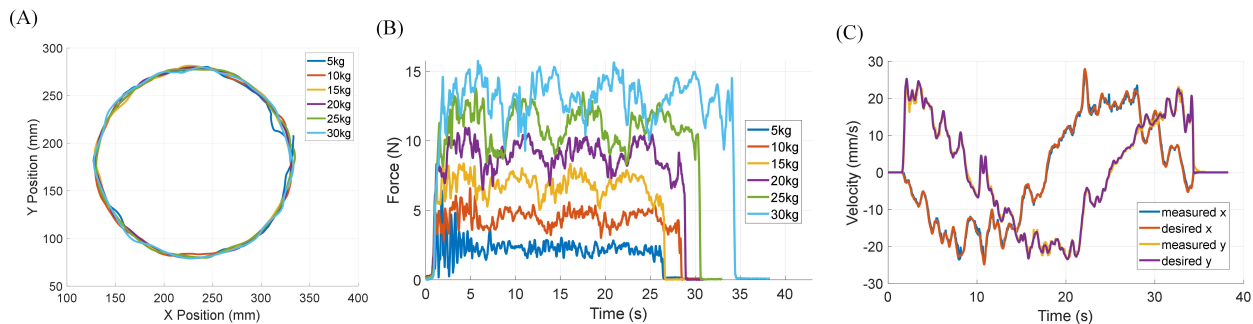


Fig. 12. Admittance Virtual Dynamics is used allowing six objects with different mass moving freely on taskspace with a friction coefficient of 0.02. The robot is set in Free Mode, a healthy subject is asked to try their best to follow a circular trajectory. (A) End-effector circular trajectory. (B) The force measured on end-effector when moving in a circular trajectory with different simulated object mass. (C) The desired and measured velocity of admittance control when moving in a circular trajectory with 30kg simulated object mass.

TABLE II

PERFORMANCE OF ADMITTANCE CONTROL SIMULATING OBJECT WITH SIX DIFFERENT MASS MOVING IN CIRCULAR TRAJECTORY UNDER FREE MODE.

Mass	5kg	10kg	15kg	20kg	25kg	30kg
Average measured end-effector force (N)	2.08	3.98	6.04	8.08	9.87	11.36
MAE of x-axis desired and measured velocity (mm/s)	2.45	0.75	0.41	0.46	0.37	0.35
MAE of y-axis desired and measured velocity (mm/s)	6.66	1	0.88	0.68	0.73	0.56

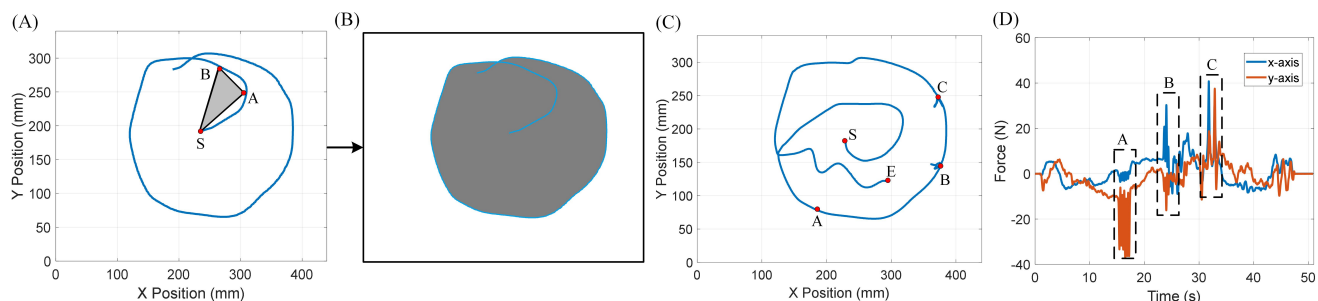


Fig. 13. Range of motion generation and evaluation in Free Mode. (A) End-effector trajectory used for range of motion generation. The end-effector trajectory colored in blue demonstrates the recorded trajectory during ROM generation. S is the starting point. A and B are end-effector positions recorded in sequence. The Motion Restriction Map is generated by drawing a triangle between the starting point S and the consecutive end-effector position. (B) The Motion Restriction Map generated by the given end-effector trajectory. The permitted areas are marked gray. (C) Random motion within permitted area in Motion Restriction Map. S is the starting point. F is the finishing point. A , B , and C are locations where the user trying to exceed the ROM limitation. (D) Force measured on the end-effector from motion in (C). Box A , B , and C are corresponding to point A , B , and C in (C).

TABLE III

HUMAN-GUIDED TRAJECTORY MODE WITH HARD BOUNDARY AND RANDOM NOISE INJECTED.

Trajectory Type	Circular	Circular	Circular	Hand-drawn	Hand-drawn	Hand-drawn
Noise magnitude	0N	3.8N	7.7N	0N	3.8N	7.7N
MAE(mm)	0.067	0.061	0.032	0.134	0.115	0.113

Force Map is generated using proposed method with a special Motion Restriction Map that has permitted area only at the center location of the taskspace. Fig. 15 (A) shows the derived impedance spring force vector field, every permitted location has an impedance spring force pointing towards the center with a magnitude proportional to the distance from the center. In Fig. 15 (B), one subject is asked to move and hold the end-effector at different locations in the impedance force zone. When the end-effector is at zero acceleration (force equilibrium), the distance between its current position and the center, as well as the current applied force on the end-effector, are recorded and plotted in Fig. 15 (B). The result

shows that the characteristic curve of simulated spring area nicely aligned with the characteristic curve of an ideal spring, which concludes that the proposed impedance control method is effective.

E. Compare To Previous Researchers

Most of previous works have the path following functionality but do not have quantitative results. Therefore we perform comparison qualitatively. Tab. IV shows the comparison between our robot and previous researcher's. The Robot-guided path following (impedance) is a trajectory following function we implemented but did not discuss in previous chapters.

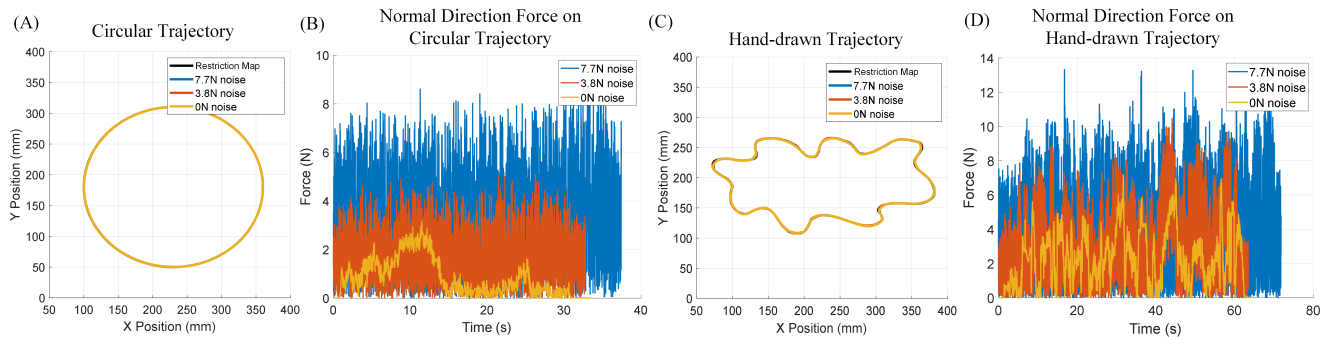


Fig. 14. Experiment using Human-guided Trajectory Mode with hard boundary and random noise injected. (A) End-effector moving on a circular trajectory Motion Restriction Map. (B) Three level of random force are injected to the end-effector force sensor as noise, results show that the IEVC is robust against noisy end-effector input forces. (C) End-effector following moving on a hand drawn trajectory Motion Restriction Map. (D) Three level of random force are injected to the end-effector force sensor as noise, results show that the IEVC is robust against noisy end-effector input forces.

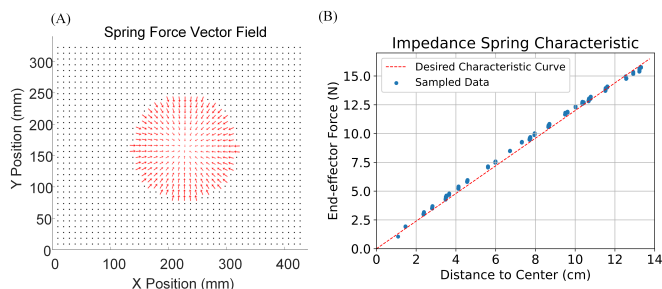


Fig. 15. Impedance force zone characteristic experiment. (A) The derived impedance spring force vector field. Every permitted location on the map has a impedance spring force pointing towards the center with a magnitude proportional to the distance from the center. (B) One subject is asked to move and hold the end-effector at different locations in the impedance force zone. When the end-effector is at zero acceleration (force equilibrium), the distance between its current position and the center, as well as the current applied force on the end-effector, are recorded and plotted.

This function use a virtual leading point that automatically marching forward on the trajectory and perform a impedance control to the end-effector which use the virtual leading point as the target. This function serve as the major functionality of previous works and can be easily accomplished by our robot by combining the Robot-guided Trajectory Mode and the Admittance Virtual Dynamics.

The proposed control method is the pioneering method that facilitates area restricted free moving and impedance-boundary free moving. Additionally, we are the first to deliver quantitative results, establishing a benchmark for future research to reference and compare.

VI. CONCLUSION

This study introduces a novel upper limb rehabilitation device, focusing on its design and control mechanisms. The device utilizes ball screws for linear actuation along the x and y axis, ensuring a simple structure and enhanced durability. Its non-backdrivable configuration enables the separation of simulated and robot dynamics, facilitating the implementation of controllers.

Three novel control algorithms are proposed. First, the Implicit Euler velocity control algorithm (IEVC) is highlighted for its state-of-the-art accuracy, stability, efficiency and generalizability in solving motion restriction control problem.

It allows for trajectory and range of motion adjustments without analytical constraints and with zero cost on additional obstacles or permitted area. Moreover, the IEVC algorithm can be adapted to any robot supporting end-effector velocity control. Second, the Admittance Virtual Dynamics simulation algorithm achieves smooth and natural human-guided motion of the non-backdrivable end-effector by simulating the motion of a virtual mass and applying this simulated motion to the end-effector. This algorithm operates with a time complexity of $O(1)$. Third, the study introduces a generalized impedance force calculation algorithm that allows impedance control on any trajectory or area boundary and operates with a runtime time complexity of $O(1)$.

The integration of the device and control algorithms results in an upper limb rehabilitation device with three distinct operation modes: Robot-guided Trajectory Mode, Free Mode, and Human-guided Trajectory Mode. These modes support stroke patients through various stages of recovery. Compared to state-of-the-art devices, the proposed device offers enhanced functionality and this paper establishes a detailed performance baseline for future research endeavors.

REFERENCES

- [1] S. S. Virani, A. Alonso, H. J. Aparicio, E. J. Benjamin, M. S. Bittencourt, C. W. Callaway, A. P. Carson, A. M. Chamberlain, S. Cheng, F. N. Delling *et al.*, "Heart disease and stroke statistics-2021 update: a report from the american heart association." 2021.
- [2] G. Kwakkel, B. J. Kollen, J. van der Grond, and A. J. Prevo, "Probability of regaining dexterity in the flaccid upper limb: impact of severity of paresis and time since onset in acute stroke," *Stroke*, vol. 34, no. 9, pp. 2181–2186, 2003.
- [3] "Inmotion arm for neurological rehabilitation." [Online]. Available: <https://bioniklabs.com/inmotion-arm/>
- [4] H. I. Krebs, M. Ferraro, S. P. Buerger, M. J. Newbery, A. Makiyama, M. Sandmann, D. Lynch, B. T. Volpe, and N. Hogan, "Rehabilitation robotics: pilot trial of a spatial extension for mit-manus," *Journal of neuroengineering and rehabilitation*, vol. 1, pp. 1–15, 2004.
- [5] K. Chua, C. Kuah, C. Ng, L. Yam, A. Budhota, S. Contu, S. Kager, A. Hussain, L. Xiang, and D. Campolo, "Clinical and kinematic evaluation of the h-man arm robot for post-stroke upper limb rehabilitation: Preliminary findings of a randomised controlled trial," *Annals of Physical and Rehabilitation Medicine*, vol. 61, p. e95, 2018, 12th World Congress of the International Society of Physical and Rehabilitation Medicine. Paris. 8-12 July 2018. [Online]. Available: <https://www.sciencedirect.com/science/article/pii/S187706571830277X>

TABLE IV
REHABILITATION DEVICE COMPARISON.

Functions	Robot-guided path following (impedance)	Robot-Guided path following (hard)	Trajectory Restricted Free Moving	Area Restricted Free Moving	Impedance Boundary Free Moving
HIT Manus [4]	Yes	No	No	No	No
Physiobot [6]	Yes	No	No	No	No
H-Man [17]	Yes	No	Yes	No	No
GARD (ours)	Yes	Yes	Yes	Yes	Yes

- [6] B. F. Villar, P. F. Viñas, J. P. Turiel, J. C. F. Marinero, and A. Gordaliza, "Influence on the user's emotional state of the graphic complexity level in virtual therapies based on a robot-assisted neuro-rehabilitation platform," *Computer Methods and Programs in Biomedicine*, vol. 190, p. 105359, 2020.
- [7] "Armmotus m2 upper limb rehabilitation robotics." [Online]. Available: <https://fourierintelligence.com/m2/>
- [8] W. H. Chang and Y.-H. Kim, "Robot-assisted therapy in stroke rehabilitation," *Journal of stroke*, vol. 15, no. 3, p. 174, 2013.
- [9] T. Johansen, L. Sørensen, K. K. Kolskär, V. Strøm, and M. F. Wouda, "Effectiveness of robot-assisted arm exercise on arm and hand function in stroke survivors—a systematic review and meta-analysis," *Journal of Rehabilitation and Assistive Technologies Engineering*, vol. 10, p. 20556683231183639, 2023.
- [10] E. C. Lu, R. Wang, R. Huq, D. Gardner, P. Karam, K. Zabjek, D. Hébert, J. Boger, and A. Mihailidis, "Development of a robotic device for upper limb stroke rehabilitation: A user-centered design approach," *Paladyn, Journal of Behavioral Robotics*, vol. 2, no. 4, pp. 176–184, 2011.
- [11] I. Díaz, J. M. Catalan, F. J. Badesa, X. Justo, L. D. Lledo, A. Ugartemendia, J. J. Gil, J. Díez, and N. García-Aracil, "Development of a robotic device for post-stroke home tele-rehabilitation," *Advances in Mechanical Engineering*, vol. 10, no. 1, p. 1687814017752302, 2018.
- [12] M. Gandolfi, N. Valè, E. K. Dimitrova, S. Mazzoleni, E. Battini, M. Filippetti, A. Picelli, A. Santamato, M. Gravina, L. Saltuari *et al.*, "Effectiveness of robot-assisted upper limb training on spasticity, function and muscle activity in chronic stroke patients treated with botulinum toxin: a randomized single-blinded controlled trial," *Frontiers in neurology*, vol. 10, p. 41, 2019.
- [13] Q. Miao, M. Zhang, Y. Wang, S. Q. Xie *et al.*, "Design and interaction control of a new bilateral upper-limb rehabilitation device," *Journal of Healthcare Engineering*, vol. 2017, 2017.
- [14] N. Ouendi, R. Hubaut, S. Pelayo, F. Anceaux, and L. Wallard, "The rehabilitation robot: factors influencing its use, advantages and limitations in clinical rehabilitation," *Disability and Rehabilitation: Assistive Technology*, vol. 19, no. 3, pp. 546–557, 2024.
- [15] A. Kerr, M. Smith, L. Reid, L. Baillie *et al.*, "Adoption of stroke rehabilitation technologies by the user community: qualitative study," *JMIR rehabilitation and assistive technologies*, vol. 5, no. 2, p. e9219, 2018.
- [16] A. Hussain, W. Dailey, C. Hughes, P. Tommasino, A. Budhota, W. K. C. Gamage, E. Burdet, and D. Campolo, "Preliminary feasibility study of the h-man planar robot for quantitative motor assessment," in *2015 IEEE/RSJ International Conference on Intelligent Robots and Systems (IROS)*. IEEE, 2015, pp. 6167–6172.
- [17] K. Maqsood, J. Luo, C. Yang, Q. Ren, and Y. Li, "Iterative learning-based path control for robot-assisted upper-limb rehabilitation," *Neural Computing and Applications*, vol. 35, no. 32, pp. 23 329–23 341, 2023.
- [18] M. Maier, B. R. Ballester, and P. F. Verschure, "Principles of neurorehabilitation after stroke based on motor learning and brain plasticity mechanisms," *Frontiers in systems neuroscience*, vol. 13, p. 74, 2019.
- [19] D. Wade, R. Langton-Hewer, V. A. Wood, C. Skilbeck, and H. Ismail, "The hemiplegic arm after stroke: measurement and recovery," *Journal of Neurology, Neurosurgery & Psychiatry*, vol. 46, no. 6, pp. 521–524, 1983.
- [20] I. Indrawati and M. Sajidin, "Active, passive, and active-assistive range of motion (rom) exercise to improve muscle strength in post stroke clients: A systematic review," in *9th International Nursing Conference, Surabaya, Indonesia*. <https://www.scitepress.org/Papers/2018/83248/83248.pdf>, 2018.
- [21] J. Veldema and P. Jansen, "Resistance training in stroke rehabilitation: systematic review and meta-analysis," *Clinical rehabilitation*, vol. 34, no. 9, pp. 1173–1197, 2020.
- [22] M. L. Turville, L. S. Cahill, T. A. Matyas, J. M. Blennerhassett, and L. M. Carey, "The effectiveness of somatosensory retraining for improving sensory function in the arm following stroke: a systematic review," *Clinical rehabilitation*, vol. 33, no. 5, pp. 834–846, 2019.
- [23] T. Fujiki and K. Tahara, "Series admittance–impedance controller for more robust and stable extension of force control," *ROBOMECH Journal*, vol. 9, no. 1, p. 23, 2022.
- [24] F. B. Hildebrand, *Introduction to numerical analysis*. Courier Corporation, 1987.